Journal of Structural Biology
December 2022, Volume 214 Issue 4 Pages 107909 (10p.)
https://doi.org/10.1016/j.jsb.2022.107909
https://archimer.ifremer.fr/doc/00800/91212/

Sub-micrometric spatial distribution of amorphous and crystalline carbonates in biogenic crystals using coherent Raman microscopy

Dicko Hamadou [1], Grünewald Tilman A. [1], Ferrand Patrick [1], Vidal-Dupiol Jeremie [2], Teaniniuraitemoana Vaihiti [3], Sham Koua Manaarii [3], Le Moullac Gilles [3], Le Luyer Jeremy [3], Saulnier Denis [3], Chamard Virginie [1], Duboisset Julien [1, *]

[1] Aix-Marseille Univ, CNRS, Centrale Marseille, Institut Fresnel, Marseille, France
[2] IHPE, Univ. Montpellier, CNRS, Ifremer, Univ. Perpignan Via Domitia, Montpellier France
[3] Ifremer, UMR 241 Environnement Insulaire Océanien (EIO), Labex Corail, Centre du Pacifique, BP 49, Vairao 98719, French Polynesia

* Corresponding author : Julien Duboisset, email address : julien.duboisset@fresnel.fr

Abstract :

In living organisms, calcium carbonate biomineralization combines complex bio-controlled physical and chemical processes to produce crystalline hierarchical hard tissues (usually calcite or aragonite) typically from an amorphous precursor phase. Understanding the nature of the successive transient amorphous phases potentially involved in the amorphous-to-crystalline transition requires characterization tools, which are able to provide a spatial and spectroscopic analysis of the biomineral structure. In this work, we present a highly sensitive coherent Raman microscopy approach, which allows one to image molecular bond concentrations in post mortem shells and living animals, by exploiting the vibrational signature of the different carbonates compounds. To this end, we target the calcium carbonate vibration mode and produce spatially and spectroscopically resolved images of the shell border of a mollusk shell, the Pinctada margaritifera pearl oyster. A novel approach is further presented to efficiently compare the amount of amorphous carbonate with respect to its crystalline counterpart. Finally, the whole microscopy method is used to image in vivo the shell border and demonstrate the feasibility and the reproducibility of the technique. These findings open chemical imaging perspectives for the study of biogenic and bio-inspired crystals.

Keywords : Coherent Raman, optical microscopy, calcium carbonate, shell oyster, crystalline transition, biomineralization

Introduction

Biomineralization, *i.e.*, the production of hierarchical mineralized tissues by living organisms, involves complex biological, chemical and physical processes (Weiner, Sagi, and Addadi 2005) able to produce, simultaneously, different crystalline polymorphs with morphological site- and species-specific architectures (O B Boggild 1930; Cuif et al. 2014). Besides being a fundamental challenge, deciphering the biomineralization mechanisms attracts the interest of scientists as it promises to provide bio-inspired strategies for the synthesis of nanostructured inorganic materials using green chemistry approaches (Yoreo et al. 2015). While it is generally understood that biomineralization escapes from classical crystallization theory, a detailed understanding of biomineralization is still lacking to date. An amorphous precursor is often involved in the biocrystallization process, as supported by the steady observation of amorphous phases within crystalline biominerals from various phyla (Beniash et al. 1997; Politi et al. 2004). For calcium carbonate ($CaCO_3$), which represents nearly 4% of the Earth's crust and is produced by sedimentation of marine species remains, several amorphous calcium carbonate (ACC) phases have been identified in biominerals, raising the question of a crystallisation pathway which involves the successive transformations of different metastable ACC compounds (Mass et al. 2017; Albéric et al. 2019). Understanding which amorphous phases are involved in the amorphous-to-crystalline transition requires characterization tools able to provide a spatial and spectroscopic analysis of the biomineral structure, ideally being compatible with *in vivo* experiment requirements. Commonly used spectroscopic techniques are either surface sensitive, like x-ray photo emission spectroscopy and Fourier transform infrared spectroscopy (Amarie et al. 2012) or rather weakly spatially resolved as nuclear magnetic resonance (Ajili et al. 2020), x-ray absorption near edge structure and extended x-ray absorption fine structure (Raz et al. 2003; Cartwright et al. 2012; Nassif et al. 2005). Raman spectroscopy can provide spatially resolved spectroscopic images but remains limited by the long acquisition time required to detect small amounts of chemical species, such as ACCs in biominerals (Masic and Weaver 2015; Habraken et al. 2015). Hence, obtaining chemical information on materials at sub-micrometric scales, in a non-destructive way and without using any labelling remains a methodological and technological challenge.

Whereas the Raman process is known to give specific chemical information based on the vibration of molecules with however a low efficiency, coherent Raman which is a highly efficient process, has been developing rapidly since the early 2000s for microscopy purpose (Zumbusch, Holtom, and Xie 1999). Based on the vibrational properties of molecules and nonlinear wave mixing processes, the coherent Raman-based techniques allow a three-

dimensional (3D) imaging of chemical bonds at video rate (Freudiger et al. 2008; Saar et al. 2010; Ozeki et al. 2012). Numerous developments have made it possible to image biological samples by targeting specific vibrations such as lipidic, amide or deuterium-carbon vibrations (Fung and Shi 2020; Cheng et al. 2002; Camp Jr and Cicerone 2015) and even to allow *in vivo* imaging (Chen et al. 2016; Evans et al. 2005; Shi et al. 2011). Mainly used for biological tissue studies, coherent Raman imaging techniques have however little been used for molecular crystals imaging (Cleff et al. 2016; Houle et al. 2017).

In this article, we demonstrate the possibility to use coherent Raman microscopy to detect and locate the presence of ACC in an as-formed $CaCO_3$ biomineral. To this aim, we target the ν_1 calcium carbonate vibration mode and produce spatially and spectroscopically resolved images of the shell border of a mollusk shell, the *Pinctada margaritifera* pearl oyster, which was chosen for the possibility to probe mineralized units at different maturity states. The article is organized as follows. In the Material and methods section, we first describe the key processes needed to understand the physics underlying coherent Raman scattering imaging and we further provide experimental details. In the Result section, Part I presents the detailed characterization of a shell border with respect to imaging and spectral analysis, exploited separately or combined. Then, a novel approach designed to efficiently evidence the amount of ACC with respect to the crystalline $CaCO_3$ counterpart is described and applied on experimental data, in Part II. Finally in Part III, we use the described method to image *in vivo* the border shell of *Pinctada margaritifera* and demonstrate the feasibility and reproducibility of the technique. Finally, our results are briefly discussed with respect to potential applications in the framework of biomineralization studies.

Material and methods

As the coherent Raman microscopy approach has never been used by other groups in the context of biomineralization studies (to the best of our knowledge), we detail hereafter the whole concept of the coherent Raman scattering process and its experimental implementations. The sample preparation details are provided at the end of the section.

Coherent Raman process

Coherent Raman is a non-linear optical process based on a coherent four-wave mixing. Such a process results from the non-linearity of the response of the probed medium to the action of strong electromagnetic fields. While most nonlinear phenomena provide lower efficiencies than linear processes, coherent Raman scattering is extremely interesting because it offers a gain in the order of 10^3 compared to the spontaneous Raman process, due to its coherent and resonant

characteristics (Petrov et al. 2007). In the coherent Raman process two electromagnetic waves, denoted pump and Stokes, of, respectively, pulsation ω_P and ω_S, amplitude A_P and A_S and wave vector k_P and k_S, are required. In order to interact with the sample, the pulsation difference of the pump and Stokes beams, namely $\Omega = \omega_P - \omega_S$, must be equal to the pulsation of the molecule vibration Ω_R (Fig. 1a). Once this condition is satisfied, several non-linear optical processes occur, as described hereafter.

(a) Coherent anti-Stokes Raman scattering

The coherent anti-Stokes Raman scattering (CARS) process generates photons at $\omega_{AS} = 2\omega_P - \omega_S$. CARS is interesting from an application point of view because the photons emitted at the pulsation ω_{AS} are blue-shifted with respect to the pump and Stokes incident fields, and thus unpolluted by a possible parasitic auto-fluorescence of the sample (Fig 1a). However, the CARS contribution is not the only one to generate photons at ω_{AS}. Indeed, another four-wave mixing contribution, named four-wave mixing or non-resonant CARS, generates photons at the same pulsation. This process comes from the instantaneous electronic response of matter and does not depend on the concentration of the targeted chemical bond. The coherent sum of these two terms modifies the spectral behavior of the anti-Stokes intensity profoundly with respect to a classical Raman profile, leading to a distortion of the spectrum and a shift of the maximum CARS intensity towards smaller wave numbers, while a minimum in the intensity profile appears at larger wavenumbers. The shape of the spectrum follows a so-called Fano profile, which results from the coupling between a system containing discrete energy levels (here, the vibrational resonances) and a system containing a continuum of energy (the non-resonant electronic response). While the CARS signal is extremely sensitive to the presence of small amounts of chemical species, it does not depend linearly on the chemical bond concentration, which makes quantitative analysis difficult to perform.

(b) Stimulated Raman scattering

To overcome the drawbacks of the CARS process, another coherent Raman process, named stimulated Raman scattering (SRS), was also proposed (Freudiger et al. 2008; Saar et al. 2010). In this process, the molecules radiate at the same pulsation as the pump and Stokes lasers (Fig. 1a). The intensity of the pump beam decreases when propagating in a medium with Raman resonance, while the Stokes beam benefits from amplification. Consequently, a transfer of energy from the pump beam to the Stokes beam is observed. If the detection device collects signal corresponding to the pump beam, the signal is referred to as the “stimulated Raman loss” (SRL) while it is called the "stimulated Raman gain” (SRG) when the signal from the Stokes

beam is collected. The major advantage of this process is that it is not polluted by a non-resonant background as observed for the CARS signal and the associated electronic response of the sample medium. The spectral information of SRG or SRL, I_{SRS}, is rigorously the same as the one of spontaneous Raman (Freudiger et al. 2008), and therefore makes it a powerful spectroscopic tool.

As for CARS, SRS microscopy allows the acquisition of hyperspectral images at video rate on biological samples (Ozeki et al. 2012). However, SRS needs a more sophisticated detection strategy. This is achieved by exploiting the laser detection, one of the lasers being modulated at a specific frequency and the detection being demodulated at the same frequency (see Fig. 1b).

Experimental implementation of coherent Raman microscopy

The implementation of a coherent Raman experiment, which is schematically depicted in Fig. 1b, requires two pulsed lasers ω_P and ω_S with precisely the same and synchronized repetition rate. Ideally at least one of the lasers must be tunable in wavelength to be able to modify the pulsation difference $\omega_P - \omega_S$ and thus to address any molecular vibrational mode. Several types of applications of coherent Raman microscopy have been reported in the literature, the most common is using optical parametric oscillators (OPO), which have the property of being tunable in pulsation (Brustlein et al. 2011). In our setup, the laser source consists of a solid state OPO pumped by a pulsation doubled Ytterbium (Yb) fiber laser (PicoEmerald, APE GmbH, Germany). The Yb laser provides the Stokes excitation beam itself, at the fixed wavelength of 1031 nm, with pulses having 2 ps duration and 80 MHz repetition rate. The pump excitation beam is generated by the OPO and can be tuned between 700 nm and 990 nm, so the system can thus scan the whole vibrational spectrum of the chemical bonds located between 400 and 4000 cm^{-1}. Whereas very short pulses are required to efficiently activate non-linear optical processes, in practice, it is preferred to use pulses with duration in the order of a few ps (10^{-12} s) to ensure a spectral resolution of a few 10 cm^{-1}. At the focal point, and with powers of a few tens of mW, the peak laser powers are sufficient to activate the pulsation mixing of the coherent Raman. The CARS signal is then detected at the pulse $\omega_{AS} = 2\omega_P - \omega_S$ using a collection lens and a sensitive photomultiplier detector. The SRS signal requires further instrumentation, involving the modulating at 20 MHz of one of the beams using electro-optic modulator (EOM) and observing the modulation transfer with a fast photodiode related to the SRS effect on the other beam through a lock-in amplifier (APE GmbH, Germany).

The efficiency of the coherent Raman processes, much larger than the one of spontaneous Raman, is exploited to perform fast imaging. The imaging properties of coherent Raman processes are the same as for other nonlinear imaging techniques (Oheim et al. 2006; Mahou et al. 2011) as *e.g.*, two-photon fluorescence imaging or second harmonic generation imaging. Indeed, coherent Raman imaging is a confocal approach, meaning that the nonlinear process is only activated inside the intense spot corresponding to the focal volume. The dimension of this spot is related to the numerical aperture of the microscope objective (Nikon, ×20, NA 0.75), *i.e.*, typically of a few hundred of nanometers laterally and of a few micrometers along the axial direction. Due to intense fields required to activate the coherent Raman process, the only imaging technique which is efficient enough is the point scanning technique (galvanometric scanner, Cambridge Technology INC): the focal volume is scanned in 3D by changing the incidence angle of the beam in the back pupil of the objective and by changing the altitude of the objective with a piezo-positioner (PIFOC, PI, Germany).

A homemade instrumental interface previously described (Ferrand 2015) ensures the synchronization between the spot scanning and the data acquisition. Typically, the image acquisition is based on scanning a 10 to 100 µm large region, with a step size of about 0.2 µm. With a typical exposure time of 80 µs per pixel, an image is delivered in a few seconds. If needed, the image quality can be improved by repeating the measurement and accumulating the individual 2D image signals. The 3D stack is further produced by moving the microscope objective along the beam path, with a step of about 0.5-1 µm.

Raman experiments

Raman spectra were acquired using a Raman spectrometer in reflection mode (LabRam HR spectrometer, Horiba) with a 100 × air objective (NA 0.9, Olympus MPlan) and a laser at 632.8 nm. The power delivered at the sample level is about 1 mW on average. The Raman spectrum is recorded using a grating of 1200 lines/mm, corresponding to a spectral window of about 500 cm^{-1} and recorded using a Peltier-cooled CCD camera. The acquisition time for each spectral window is 1 min for the geological calcite crystal.

Sample preparation - *Post mortem* samples

The juvenile *Pinctada margaritifera* (*Pm*) shells were farmed at the IFREMER hatchery at the biological station of Vairao (Tahiti). They were cultivated in an optimal and sanitary-controlled environment to avoid any contamination during growth. Once selected, they were preserved in

a 70% ethanol/water solution and transferred to Institut Fresnel (Marseille, France). The shells are about 7-20 mm long. Regions in the vicinity of the growing edge of the shell, extending over 1-2 mm, were chosen for the analysis. The shell edge presents a continuous growth history with the bulk of the shell being composed of well-developed and tightly packed prisms (typical size of about 20 μm), while the growth edge exhibits isolated, smaller, and rather disc-like units, which we refer to as discs. Those are the early stages of the prismatic units (Duboisset et al. 2022). For the coherent Raman investigations, the shells were cut into pieces of about 1 mm^2 and placed onto a microscopy glass slide, in an ethanol/water solution. The threshold of beam-induced damage has been determined on a different region on the sample and a power of about 50% of the threshold value was used to avoid beam-induced damage.

Sample preparation - *In vivo* samples

The living animals were sent from the biological station of Vairao (Tahiti), to Institut Fresnel by express delivery. During the travel, they were kept in air at room temperature. At their arrival, they were transferred into a seawater aquarium (T = 28°C, pH = 8.24, kH = 7.6, [Ca] = 400 ppm, [Mg] = 1350 ppm, [NaCl] = 35g/L) and fed regularly with fresh algae. Three weeks after their arrivals, some of them were mounted onto an optical glass plate, using a combination of bio-compatible epoxy putty (Coralscaper, Arka Biotech, Germany) and a biocompatible aquarium glue (Orca Underwater Glue, Aquarium Münster, Germany). They were further stored in the aquarium for a few more days, before the first coherent Raman microscopy investigation was performed. A cell (volume of about 100 cm^3) was designed to perform coherent Raman experiments with the animal on the glass plate. The cell was connected to the aquarium through two tubes allowing the inflow and outflow of water and ensuring the submersion of the animal under a constant flow of water. The water debit into the cell was monitored with a peristaltic pump and adjusted to 100 mL/min.

Results

Part I - Coherent Raman scattering imaging

(a) Structural properties

Figure 2 depicts images obtained in the SRS mode and acquired at the growth edge of a *Pinctada margaritifera* shell. The laser pulsation difference was fixed to the υ_1 Raman carbonate vibration of calcite ($\upsilon_1 = 1086$ cm^{-1}, with $\nu_1 = \frac{\Omega_R}{2\pi c}$ where c is the speed of light). In Fig. 2a and b, the 3D stack is integrated along the beam propagation direction to increase the

signal-to-noise ratio, while Fig. 2c presents a 2D cross-section allowing the visualization of the shell along its thickness. The mature prisms (juxtaposed polygons), young prisms (partly rounded prisms) and young discs are well visible, observed from the umbo of the shell towards the shell edge. The 2D spatial resolution of the coherent Raman microscope is demonstrated in the planar view of Fig 2b: on this image, each pixel corresponds to an area of 200 × 200 nm^2. The resolution of the imaging set-up allows the observation of carbonate-poor ring structures, inside the prism, presenting a gap of size well below one micrometer. Fine carbonate density fluctuations are also observed. Fig. 2c, which depicts a 2D cross-section extracted from the 3D stack, evidences the degradation of the spatial resolution along the beam propagation direction, due to the focal volume length, longer in the axial direction with respect to the lateral direction. Along this direction, which corresponds also to the thickness direction of the shell, the image resolution is in the order of 2-3µm, making it difficult to resolve structures below this limit. However, a clear decrease of the shell thickness can be observed, evidenced by the envelope of the signal and by the decrease of the SRS signal intensity while approaching the shell edge.

(b) Spectral properties

The wavelength of the second OPO can be changed, offering the ability to probe a spectral domain around the calcite υ_1 wavenumber. Scanning the laser wavelength in steps of 0.1 nm corresponds to a wavenumber shift of about 1 cm^{-1}, in this domain. However, the spectral resolution of CARS and SRS differs from the Raman spectral resolution. The latter one is defined by the laser bandwidth and grating resolution and is typically in the 0.1 cm^{-1} range. For coherent Raman, due to the intense electromagnetic field required to generate the CARS or SRS process, pulsed lasers are used for their capability to deliver large intensity illumination. This comes with a drawback, as the limited temporal duration of the pulse results in a large spectral width, of a few fractions of nm, which corresponds to a spectral bandwidth of more than 10 cm^{-1}. Consequently, even if the laser maximum wavelength can be shifted by a few cm^{-1}, the spectral resolution of the coherent Raman spectrum is rather broad. This is experimentally illustrated in Fig. 3, which compares the spontaneous Raman spectrum of a geological calcite crystal to the spectra obtained with CARS and SRS, for the same calcite crystal, in the vicinity of υ_1. Here, geological calcite has been chosen for its known sharp spectrum profile, which allowed us to characterize the performance of coherent Raman spectroscopy. The spontaneous Raman spectrum exhibits a Full Width at Half Maximum (FWHM) of 2 cm^{-1}, resulting mostly from the geological calcite purity. The CARS and SRS FWHM spectra are much broader, with

a FWHM of 12 cm^{-1} for SRS and 18 cm^{-1} for CARS, due to the intrinsic spectral broadening of the lasers. Worth to notice, the SRS spectrum presents a shape rather similar to the Raman spectrum profile, whereas the CARS spectrum is asymmetric and slightly shifted towards the low wavenumbers regime due to the interaction with the non-resonant background, as described in the Material and methods section. The consequence is the observation of a CARS intensity maximum at about 1081 cm^{-1} instead of the expected value of 1086 cm^{-1}. This preliminary spectral analysis allowed us to highlight the spectral performance (and limits) of CARS and SRS with respect to classical Raman. In the following, we present the spectral investigation of the shell biomineral.

(c) Hyperspectral imaging

Combining the imaging and spectral modalities of coherent Raman, a hyperspectral characterization of the shell sample can be carried out: for each wavenumber, a 3D image of the sample is acquired, meaning that each voxel of the 3D image volume contains spectral information. Fig. 4 depicts CARS and SRS images recorded simultaneously for several wavenumbers around υ_1. Close to υ_1, the signal arising from the $CaCO_3$ mineralized units is brighter and the contrast between the units and the surrounding media is larger, while the response of the surrounding media remains rather constant over the spectral investigation.

Two CARS (resp., SRS spectra), shown in Fig. 4a (resp., b) are further extracted from the hyperspectral images, in regions defined in Fig. 4c (resp., d) and corresponding to a disc (red circle) and a prism (blue circle). The CARS spectra present the expected behavior, *i. e.*, asymmetry and shift towards lower wavenumbers. It is worth to notice that the shift is more pronounced for the disc, an artifact which is linked to the small amount of $CaCO_3$ in the thin disc, resulting in strongest impact of the cross-term of the CARS intensity expression (*i.e.*, the mixing between the non-resonant and resonant contributions). On the larger wavenumbers side, the CARS signal presents a destructive interference between the resonant and the non-resonant four wave-mixing, providing a signal intensity lower than the surrounding background. From these observations, a quantitative characterization of the $CaCO_3$ distribution from the CARS modality is difficult, although CARS microscopy demonstrates good performances for the detection of chemical species with low concentration levels. The SRS spectra (Fig. 4b) present a signal maximum at the υ_1 value, as expected. Other maxima are also visible in the low wavenumber region, at about 1074 cm^{-1}. It can be assigned to other carbonate vibrations, such as free carbonate vibration or hydrated-carbonate vibration (Coleyshaw, Crump, and Griffith 2003). A large number of studies has reported the peak shift of carbonate vibration as a function

of its close environment (De La Pierre et al. 2014; Tlili et al. 2002). In biominerals, the observation of a broad peak of about 30 cm^{-1} is often attributed to an amorphous calcium carbonate phase (Addadi, Raz, and Weiner 2003). Therefore, in the following, we refer to the observed low wavenumber signal (at about 1074 cm^{-1}) as ACC while the crystalline contribution at 1086 cm^{-1} is referred to as Cal for calcite. We note that the low spectral resolution of coherent Raman scattering does not allow an accurate assignments of this low wavenumber peak. In addition, the two contributions, Cal and ACC, being spectrally close one to the other, it makes it difficult to extract their individual contributions without a detailed fit of the spectra collected over the imaged area, therefore necessitating a detailed spectral investigation of the sample in the vicinity of the ν_1 vibration. In the next part, we propose an analysis routine developed to quantify the relative spatial contribution of the two components, exploiting a limited amount of data.

Part II - Coherent Raman data analysis

(a) Definition of an intensity-based contrast

In order to quantify the ACC and Cal contributions we developed an analysis routine based on the calculation of the symmetric difference map. This contrast map, C, corresponds to the difference between the intensity maps measured at the two selected wavenumbers, namely I_{Cal} and I_{ACC}, normalized by the sum of the two intensity maps. It formally reads

$$C = (I_{Cal} - \gamma I_{ACC}) / (I_{Cal} + \gamma I_{ACC}). \quad (4)$$

with γ a weighting factor that accounts for the width difference between the two Raman peaks. As detailed in the appendix, it formally reads as $\gamma = W_{ACC}/W_{Cal}$, with W_{Cal} and W_{ACC} the width of the Cal and ACC peaks, respectively. When Cal is taken as the reference, a signal fully dominated by the Cal (resp., ACC) contribution result to C = +1 (resp., -1), while the value C = 0 would indicate equivalent contributions of Cal and ACC. Note that C is a unit-less value. We show hereafter that C is able to depict the spatial variations of Cal and ACC in their relative distributions.

In order to test the relevance of this approach, we developed a numerical model shown in Fig. 5. The SRS experimental spectrum of the ν_1 calcite resonance is described by a Gaussian function, centered at 1086 cm^{-1}, and presenting a FWHM W_{Cal} equals to 10 cm^{-1} (Fig. 5a). The ACC resonance is described by a similar peak profile (W_{ACC} = 20 cm^{-1}, centered at 1074 cm^{-1}, Fig. 5b). From this, a global spectrum can be calculated (Fig. 5c), for a series of Cal and ACC quantities, ranging from only Cal to only ACC contributions. The respective Cal and ACC

quantities are referred to as [Cal] and [ACC]. They correspond to a relative concentration of Cal and ACC, respectively. The exact quantity contrast C_q is defined as the ratio

$$C_q = ([Cal] - [ACC]) / ([Cal] + [ACC]). \quad (5)$$

From this definition, C_q was calculated for various ([Cal], [ACC]) combinations. A value of C_q = +1 (resp., -1), indicates the exclusive presence of Cal (resp., ACC), while C_q = 0 means that [Cal] = [ACC]. This map should be compared to the C map, produced with eq. (4) using $\gamma = 2$, extracted from the spectra simulation (both maps shown in Fig. 5d and e). It shows a behavior similar to C_q, furthermore illustrated by the calculation of the difference between C and C_q (Fig. 5f). Some negligible discrepancies are however observed when [Cal] is close to 0.

At this stage, several remarks can be made. Note that if a non-resonant (constant) background is added to the spectrum, the whole C amplitude is reduced. In other words, in the case where only Cal (resp., ACC) would be present in the investigated volume, C would no longer be equal to +1 (resp., -1) but would decrease down to $(1+2B/I_{Cal})^{-1}$ (resp., $-(1+2B/I_{ACC})^{-1}$), with B the non-resonant background level. This however preserves the monotonic behavior of C with respect to [Cal] and [ACC], ensuring that two different positions on the sample can still be compared and analyzed. In addition, if the peak widths associated to the Cal and ACC phases are different (*e.g.*, the ACC peak is much broader), the whole C value is shifted. Here again, the monotonic behavior of C with respect to [Cal] and [ACC] is preserved, but C = 0 does no longer mean that [Cal] = [ACC]. This effect can easily be accounted for in the expression of C by adjusting the γ, as long as the relative width of the peaks is known and invariant over the investigated region. In the absence of detailed knowledge of the respective peak widths (in this case, γ can be set to 1), we note however that the whole C behavior follows the behavior of C_q and is therefore suitable to monitor local variations in the balance of [Cal] vs [ACC], in a specimen.

(b) Contrast map analysis at the shell edge

In Fig. 6, we further illustrate the method shown above with the analysis of experimental data acquired at the *Pm* shell edges (Fig. 4). Fig. 6b shows the contrast map calculated with eq. (4), obtained from the SRS intensity data acquired at 1086 and 1074 cm^{-1}. As a matter of comparison, the C_q map, resulting from the fit of the spectrum profile (Fig. 6a) in each point of the shell border, is shown in Fig. 6c. The fit model required two chemical contributions, centered around 1086 and 1074 cm^{-1}, respectively. Different fit parameters were tested, leading to minor variations of the values. The FWHM of the individual peaks was fixed to about 10

cm^{-1} for Cal and 20 cm^{-1} for ACC, and a non-resonant (spectrally invariant) background was added to the model. The amplitude of the peaks and the exact peak positions were let free during the fit (at least within a limited spectral window of about 5 cm^{-1}, for these latter ones). The C_q map is extracted by using the peak amplitudes of the Cal and ACC peak contributions, as obtained from the fit of the experimental data. A very good relative agreement is observed between C_q and C (Fig. 6d), confirming that the C map can be used to qualitatively evaluate the relative presence of ACC, in this calcium carbonate biomineral sample. The small mismatch (lower than 30%) likely results from the presence of an additional non-resonant background and/or from a different peak width for the ACC contribution. However, the major information regarding the spatial distribution of ACC within this shell can be extracted with confidence. While the prisms and young discs are rather homogeneous, being composed mostly of crystalline material, a small portion of ACC-rich material is observed at their periphery. It was previously interpreted as the onset of a radial crystallization front, progressing from the center to the border of the mineralizing unit (Duboisset et al. 2022). The observed ACC would be the leftover of the arrested crystallization process.

III - Coherent Raman microscopy applied to *in vivo* mollusk shell study

To provide a final illustration of the interest of coherent Raman microscopy in the framework of biomineral and biomaterial related questions, we describe below the results of an *in vivo* experiment, performed with a living *Pm* specimen. To this aim, an optically transparent cell was designed and mounted onto the coherent Raman microscope, allowing for a constant seawater (+ food) flux during the optical observation (Fig. 7a). The *Pm* mollusk shell was glued onto the glass plate to ensure stability of the animal. Thus, one valve was maintained aligned to the glass slide, while the second one could freely open during the animal activity. Figure 7b shows the white light image (between crossed polarizers) of the shell border. The individual prisms exhibit a birefringent contrast, resulting from their optical and geometrical properties (Baroni, Chamard, and Ferrand 2020). The mantle of the animal is retracted inside the shell (black part on the left) and the border is fully visible. The SRS images were obtained in the vicinity of the shell border, on the valve close to the glass plate (see the highlighted region in Fig. 7b), at two different times, named t_0 and t_1, with $t_1 = t_0 + 3$ days. After the first experiment, the shell was placed back in the aquarium and maintained alive. After 3 days, the *in vivo* coherent microscopy investigation was repeated (Figs. 7c and d). The Cal wavenumber and the ACC wavenumber images were recorded each time. As previously observed in the *post mortem* study, the shell edge exhibits distinct juxtaposed mature prisms and younger discs. We note that

the total intensity of the signal at t_0 is slightly lower than the signal recovered at t_1 due to a reduce laser power during the acquisition. Interestingly, this general intensity fluctuation shall not affect the relative behavior of C. The C maps, obtained by comparing the Cal image and ACC image (data not shown) are shown in Fig. 7e and f, for t_0 and t_1, respectively. To demonstrate the repeatability of the measurements, histograms of the C maps are extracted from two regions of interest referred to as ROI 1 (mature prism) and ROI 2 (young disc) and further depicted in Figs. 7g and h. The average values of C for each ROIs, at t_0 and t_1, are the same. This demonstrates the good reproducibility of the experimental approach, confirming that the observation probe did not damage the shell and that no additional bias was present. The standard deviation of the histogram is clearly higher at t_0 because the total intensity magnitude is weaker. Indeed, the error on C, namely ΔC, depends on a first approximation to

$$\Delta C \approx \frac{\Delta I_{Cal} + \gamma\, \Delta I_{ACC}}{I_{Cal} + \gamma I_{ACC}} \tag{6}$$

where ΔI_{Cal} and ΔI_{ACC} are the standard deviations of the Cal and ACC signal magnitudes. The standard deviations calculated from eq. 6 are represented in Figs. 7g-h (horizontal bars). They fully follow the experimental shapes of the histograms.

IV - Discussion - conclusions

In this experimental work, we show the potential of this microscopy method in the specific case of calcareous biominerals. As coherent Raman microscopes are becoming accessible worldwide, this work shall be relevant for the design of new research strategies. As a first result, we produced spatially highly-resolved images of a mollusk shell edge, allowing the detailed investigation of the distribution of the carbonates linked to the calcite phase, over a large shell area.

The spectral investigation of this sample, performed with CARS and SRS, highlights the strengths and weaknesses of both approaches. CARS is highly sensitive and able to detect small amounts of a given chemical bond, as shown by the intensity maximum of the spectrum extracted from a thin disc, compared to the intensity maximum extracted from a mature thick prism, which is only about 20% larger than the signal arising from the much thinner disc. However, the CARS spectrum may be highly distorted by the coherent mixing with the non-resonant background, on the one hand, and from the presence of two chemical species of close wavenumbers, on the other hand. This second effect being dependent on the relative presence of the two species, it makes it difficult to produce (even only qualitative) maps of the relative contributions of the two species, unless a full spectral model is derived and fitted to the data.

SRS, in a spectral modality approach, produces spectra in close agreement with the spontaneous Raman response, with however a comparatively poor spectral resolution. In order to go further in the spectral analysis, fits of the full spectral data set can be performed, for each point of the 2D image. Here, two contributions were needed to account for the full spectral profile. While the first one could safely be attributed to calcite, the second one, at lower wavenumbers could correspond to ACC and calcium carbonates related compounds, known to shift the ν_1 resonance mode towards lower wavenumbers. Identifying these phases further, as well as discussing the exact nature of the ACC polyamorph is out of the scope of the present work and will be further studied in a future article. We further introduced the calculation of the contrast C, which is able to highlight the relative spatial distribution of crystalline calcite and ACC, using only two sets of data at the expected Cal and ACC wavenumber values. The fair agreement between C and its exact counterpart, based on the extractions of the respective concentrations from a fit model, confirms the interest of C in the context of fast and weakly invasive sample characterization. Hence, this approach, coherent Raman microscopy performed at two relevant wavenumbers, is sufficiently fast to become compatible with the follow-up of an evolving sample.

Finally, we showed that coherent microscopy could be applied to the study of small living animals, such as mollusk. Our first test experiment confirmed the reproducibility of the method and its compatibility with a living mollusk shell. The presence of ACC-rich regions could be observed in the *in vivo* experiment, confirming the relevance of the ACC phase as a precursor of the biomineral calcite, as proposed earlier (Weiss et al. 2002; Addadi, Raz, and Weiner 2003; Nassif et al. 2005; DeVol et al. 2015; Duboisset et al. 2022). In a next step, a more detailed temporal follows up of the ACC to calcite transformation should be performed, by measuring the spatially resolved SRS signals at the relevant wavenumbers, *i.e.*, 1074 and 1086 cm^{-1}, during the mineralizing cycles of the mollusk. This opens up exciting new perspectives for the study of biomineralization and, furthermore, other phase transformation related problems.

Appendix

Here we briefly describe the derivation of the γ factor introduced in Eq. 4. In presence of the two concentrations of species [Cal] and [ACC], the measured Raman intensity writes in this spectral region as a weighted sum on the two spectra

$$\mathrm{I}(\nu) = [Cal]\mathrm{G}(\nu)_{1086,W_{Cal}} + [\mathrm{ACC}]\mathrm{G}(\nu)_{1074,W_{ACC}} \quad (7)$$

where $\mathrm{G}(\nu)_{\nu_0,W} = \frac{1}{W\sqrt{2\pi}}\exp\left(-\frac{(\nu-\nu_0)^2}{2\mathrm{W}^2}\right)$ is the normalized Gaussian distribution centered at ν_0 of width W. Defining the contrast C as in Eq. 4 gives

$$\mathrm{C} = \frac{\mathrm{I}(1086) - \gamma \mathrm{I}(1074)}{\mathrm{I}(1086) + \gamma \mathrm{I}(1074)} \approx \frac{[\mathrm{Cal}]\mathrm{G}_{1086,\mathrm{W_{Cal}}}(1086) - \gamma[\mathrm{ACC}]\mathrm{G}_{1074,\mathrm{W_{ACC}}}(1074)}{[\mathrm{Cal}]\mathrm{G}_{1086,\mathrm{W_{Cal}}}(1086) + \gamma[\mathrm{ACC}]\mathrm{G}_{1074,\mathrm{W_{ACC}}}(1074)} \quad (8)$$

where we have assumed that the cross-talk between the two Raman peaks was negligeable, *i. e.*, $\mathrm{G}_{1086,\mathrm{W_{Cal}}}(1074) \approx 0$ and $\mathrm{G}_{1074,\mathrm{W_{ACC}}}(1086) \approx 0$. Given that $\frac{G_{1074,W_{ACC}}(1074)}{G_{1086,W_{Cal}}(1086)} = \frac{W_{Cal}}{W_{ACC}}$, one can easily show that Eq. 8 can be written as

$$\mathrm{C} \approx \frac{[\mathrm{Cal}] - \gamma \frac{W_{Cal}}{W_{ACC}}[\mathrm{ACC}]}{[\mathrm{Cal}] + \gamma \frac{W_{Cal}}{W_{ACC}}[\mathrm{ACC}]}, \quad (9)$$

so that the right term equals C_q if $\gamma = \frac{W_{ACC}}{W_{Cal}}$.

Acknowledgment
This work received funding from the European Research Council (European Union's Horizon H2020 research and innovation program grant agreement No 724881).

Bibliography

Addadi, L., S. Raz, and S. Weiner. 2003. "Taking Advantage of Disorder: Amorphous Calcium Carbonate and Its Roles in Biomineralization." *Advanced Materials* 15 (12): 959–70. https://doi.org/10.1002/adma.200300381.

Ajili, Widad, Guillaume P. Laurent, Nicolas Menguy, Axel Gansmuller, Sylvain Huchette, Stéphanie Auzoux-Bordenave, Nadine Nassif, and Thierry Azais. 2020. "Chemical Heterogeneities within the Disordered Mineral Domains of Aragonite Platelets in Nacre from the European Abalone Haliotis Tuberculata." *The Journal of Physical Chemistry C* 124 (26): 14118–30. https://doi.org/10.1021/acs.jpcc.0c00280.

Albéric, Marie, Cayla A. Stifler, Zhaoyong Zou, Chang-Yu Sun, Christopher E. Killian, Sergio Valencia, Mohamad-Assaad Mawass, Luca Bertinetti, Pupa U. P. A. Gilbert, and Yael Politi. 2019. "Growth and Regrowth of Adult Sea Urchin Spines Involve Hydrated and Anhydrous Amorphous Calcium Carbonate Precursors." *Journal of Structural Biology: X* 1 (January): 100004. https://doi.org/10.1016/j.yjsbx.2019.100004.

Amarie, Sergiu, Paul Zaslansky, Yusuke Kajihara, Erika Griesshaber, Wolfgang W. Schmahl, and Fritz Keilmann. 2012. "Nano-FTIR Chemical Mapping of Minerals in Biological Materials." *Beilstein Journal of Nanotechnology* 3: 312–23. https://doi.org/10.3762/bjnano.3.35.

Baroni, Arthur, Virginie Chamard, and Patrick Ferrand. 2020. "Extending Quantitative Phase Imaging to Polarization-Sensitive Materials." *Physical Review Applied* 13 (5): 054028. https://doi.org/10.1103/PhysRevApplied.13.054028.

Beniash, E., J. Aizenberg, L. Addadi, and S. Weiner. 1997. "Amorphous Calcium Carbonate Transforms into Calcite during Sea Urchin Larval Spicule Growth." *Proceedings of the Royal Society B: Biological Sciences* 264 (1380): 461–65. https://doi.org/10.1098/rspb.1997.0066.

Brustlein, Sophie, Patrick Ferrand, Nico Walther, Sophie Brasselet, Cyrille Billaudeau, Didier Marguet, and Hervé Rigneault. 2011. "Optical Parametric Oscillator-Based Light Source for Coherent Raman Scattering Microscopy: Practical Overview." *Journal of Biomedical Optics* 16 (2): 021106. https://doi.org/10.1117/1.3533311.

Camp Jr, Charles H., and Marcus T. Cicerone. 2015. "Chemically Sensitive Bioimaging with Coherent Raman Scattering." *Nature Photonics* 9 (5): 295–305. https://doi.org/10.1038/nphoton.2015.60.

Cartwright, Julyan H. E., Antonio G. Checa, Julian D. Gale, Denis Gebauer, and C. Ignacio Sainz-Díaz. 2012. "Calcium Carbonate Polyamorphism and Its Role in Biomineralization: How Many Amorphous Calcium Carbonates Are There?" *Angewandte Chemie International Edition* 51 (48): 11960–70. https://doi.org/10.1002/anie.201203125.

Chen, X., P. Gasecka, F. Formanek, J.-B. Galey, and H. Rigneault. 2016. "In Vivo Single Human Sweat Gland Activity Monitoring Using Coherent Anti-Stokes Raman Scattering and Two-Photon Excited Autofluorescence Microscopy." *British Journal of Dermatology* 174 (4): 803–12. https://doi.org/10.1111/bjd.14292.

Cheng, Ji-Xin, Y. Kevin Jia, Gengfeng Zheng, and X. Sunney Xie. 2002. "Laser-Scanning Coherent Anti-Stokes Raman Scattering Microscopy and Applications to Cell Biology." *Biophysical Journal* 83 (1): 502–9. https://doi.org/10.1016/S0006-3495(02)75186-2.

Cleff, Carsten, Alicja Gasecka, Patrick Ferrand, Hervé Rigneault, Sophie Brasselet, and Julien Duboisset. 2016. "Direct Imaging of Molecular Symmetry by Coherent Anti-Stokes Raman Scattering." *Nature Communications* 7.

Coleyshaw, Esther E, Gregory Crump, and William P Griffith. 2003. "Vibrational Spectra of the Hydrated Carbonate Minerals Ikaite, Monohydrocalcite, Lansfordite and Nesquehonite." *Spectrochimica Acta Part A: Molecular and Biomolecular*

Spectroscopy, Georaman 2002, Fifth International Conference on Raman Spectroscopy Applied to the Earth Sciences, 59 (10): 2231–39. https://doi.org/10.1016/S1386-1425(03)00067-2.

Cuif, Jean-Pierre, Manfred Burghammer, Virginie Chamard, Yannicke Dauphin, Pierre Godard, Gilles Moullac, Gernot Nehrke, and Alberto Perez-Huerta. 2014. "Evidence of a Biological Control over Origin, Growth and End of the Calcite Prisms in the Shells of Pinctada Margaritifera (Pelecypod, Pterioidea)." *Minerals* 4 (December): 815–34. https://doi.org/Cuif, J. P. , Burghammer, M. , Chamard, V. , Dauphin, Y. , Godard, P. , Moullac, G. , Nehrke, G. ORCID: https://orcid.org/0000-0002-2851-3049 <https://orcid.org/0000-0002-2851-3049> and Perez-Huerta, A. (2014) Evidence of a Biological Control over Origin, Growth and End of the Calcite Prisms in the Shells of Pinctada margaritifera (Pelecypod, Pterioidea) , Minerals, 4 (4), pp. 815-834 . doi:https://doi.org/10.3390/min4040815 <https://doi.org/10.3390/min4040815> , hdl:10013/epic.44741.

De La Pierre, Marco, Cédric Carteret, Lorenzo Maschio, Erwan André, Roberto Orlando, and Roberto Dovesi. 2014. "The Raman Spectrum of CaCO3 Polymorphs Calcite and Aragonite: A Combined Experimental and Computational Study." *The Journal of Chemical Physics* 140 (16): 164509. https://doi.org/10.1063/1.4871900.

DeVol, Ross T., Chang-Yu Sun, Matthew A. Marcus, Susan N. Coppersmith, Satish C. B. Myneni, and Pupa U.P.A. Gilbert. 2015. "Nanoscale Transforming Mineral Phases in Fresh Nacre." *Journal of the American Chemical Society* 137 (41): 13325–33. https://doi.org/10.1021/jacs.5b07931.

Duboisset, Julien, Patrick Ferrand, Arthur Baroni, Tilman A. Grünewald, Hamadou Dicko, Olivier Grauby, Jeremie Vidal-Dupiol, et al. 2022. "Amorphous-to-Crystal Transition in the Layer-by-Layer Growth of Bivalve Shell Prisms." *Acta Biomaterialia* 142 (April): 194–207. https://doi.org/10.1016/j.actbio.2022.01.024.

Evans, Conor L., Eric O. Potma, Mehron Puoris'haag, Daniel Côté, Charles P. Lin, and X. Sunney Xie. 2005. "Chemical Imaging of Tissue in Vivo with Video-Rate Coherent Anti-Stokes Raman Scattering Microscopy." *Proceedings of the National Academy of Sciences* 102 (46): 16807–12. https://doi.org/10.1073/pnas.0508282102.

Ferrand, Patrick. 2015. "GPScan.VI: A General-Purpose LabVIEW Program for Scanning Imaging or Any Application Requiring Synchronous Analog Voltage Generation and Data Acquisition." *Computer Physics Communications* 192 (July): 342–47. https://doi.org/10.1016/j.cpc.2015.03.010.

Freudiger, Christian W., Wei Min, Brian G. Saar, Sijia Lu, Gary R. Holtom, Chengwei He, Jason C. Tsai, Jing X. Kang, and X. Sunney Xie. 2008. "Label-Free Biomedical Imaging with High Sensitivity by Stimulated Raman Scattering Microscopy." *Science* 322 (5909): 1857–61. https://doi.org/10.1126/science.1165758.

Fung, Anthony A., and Lingyan Shi. 2020. "Mammalian Cell and Tissue Imaging Using Raman and Coherent Raman Microscopy." *WIREs Systems Biology and Medicine* 12 (6): e1501. https://doi.org/10.1002/wsbm.1501.

Habraken, Wouter J. E. M., Admir Masic, Luca Bertinetti, Ali Al-Sawalmih, Lilah Glazer, Shmuel Bentov, Peter Fratzl, Amir Sagi, Barbara Aichmayer, and Amir Berman. 2015. "Layered Growth of Crayfish Gastrolith: About the Stability of Amorphous Calcium Carbonate and Role of Additives." *Journal of Structural Biology* 189 (1): 28–36. https://doi.org/10.1016/j.jsb.2014.11.003.

Houle, Marie-Andrée, Robert C. Burruss, Andrew Ridsdale, Douglas J. Moffatt, François Légaré, and Albert Stolow. 2017. "Rapid 3D Chemical-Specific Imaging of Minerals Using Stimulated Raman Scattering Microscopy." *Journal of Raman Spectroscopy* 48 (5): 726–35. https://doi.org/10.1002/jrs.5098.

Mahou, Pierre, Nicolas Olivier, Guillaume Labroille, Louise Duloquin, Jean-Marc Sintes, Nadine Peyriéras, Renaud Legouis, Delphine Débarre, and Emmanuel Beaurepaire. 2011. "Combined Third-Harmonic Generation and Four-Wave Mixing Microscopy of Tissues and Embryos." *Biomedical Optics Express* 2 (10): 2837–49. https://doi.org/10.1364/BOE.2.002837.

Masic, Admir, and James C. Weaver. 2015. "Large Area Sub-Micron Chemical Imaging of Magnesium in Sea Urchin Teeth." *Journal of Structural Biology* 189 (3): 269–75. https://doi.org/10.1016/j.jsb.2014.12.005.

Mass, Tali, Anthony J. Giuffre, Chang-Yu Sun, Cayla A. Stifler, Matthew J. Frazier, Maayan Neder, Nobumichi Tamura, Camelia V. Stan, Matthew A. Marcus, and Pupa U. P. A. Gilbert. 2017. "Amorphous Calcium Carbonate Particles Form Coral Skeletons." *Proceedings of the National Academy of Sciences* 114 (37): E7670–78. https://doi.org/10.1073/pnas.1707890114.

Nassif, Nadine, Nicola Pinna, Nicole Gehrke, Markus Antonietti, Christian Jäger, and Helmut Cölfen. 2005. "Amorphous Layer around Aragonite Platelets in Nacre." *Proceedings of the National Academy of Sciences* 102 (36): 12653–55. https://doi.org/10.1073/pnas.0502577102.

O B Boggild. 1930. "The Shell Structure of the Mollusks." In , 2:231–36. Kgl Dan. Vidensk Selsk Skr Natruvidensk Og Mathem.

Oheim, Martin, Darren J. Michael, Matthias Geisbauer, Dorte Madsen, and Robert H. Chow. 2006. "Principles of Two-Photon Excitation Fluorescence Microscopy and Other Nonlinear Imaging Approaches." *Advanced Drug Delivery Reviews*, Multi-Photon Imaging: Diseases and Therapies, 58 (7): 788–808. https://doi.org/10.1016/j.addr.2006.07.005.

Ozeki, Yasuyuki, Wataru Umemura, Yoichi Otsuka, Shuya Satoh, Hiroyuki Hashimoto, Kazuhiko Sumimura, Norihiko Nishizawa, Kiichi Fukui, and Kazuyoshi Itoh. 2012. "High-Speed Molecular Spectral Imaging of Tissue with Stimulated Raman Scattering." *Nature Photonics* 6 (12): 845–51. https://doi.org/10.1038/nphoton.2012.263.

Petrov, Georgi I., Rajan Arora, Vladislav V. Yakovlev, Xi Wang, Alexei V. Sokolov, and Marlan O. Scully. 2007. "Comparison of Coherent and Spontaneous Raman Microspectroscopies for Noninvasive Detection of Single Bacterial Endospores." *Proceedings of the National Academy of Sciences* 104 (19): 7776–79. https://doi.org/10.1073/pnas.0702107104.

Politi, Yael, Talmon Arad, Eugenia Klein, Steve Weiner, and Lia Addadi. 2004. "Sea Urchin Spine Calcite Forms via a Transient Amorphous Calcium Carbonate Phase." *Science*, November. https://doi.org/10.1126/science.1102289.

Raz, S., P.c. Hamilton, F.h. Wilt, S. Weiner, and L. Addadi. 2003. "The Transient Phase of Amorphous Calcium Carbonate in Sea Urchin Larval Spicules: The Involvement of Proteins and Magnesium Ions in Its Formation and Stabilization." *Advanced Functional Materials* 13 (6): 480–86. https://doi.org/10.1002/adfm.200304285.

Saar, Brian G., Christian W. Freudiger, C. Michael Stanley, Gary R. Holtom, and X. Sunney Xie. 2010. "Video-Rate Molecular Imaging In Vivo with Stimulated Raman Scattering." *Science (New York, N.Y.)* 330 (6009): 1368–70. https://doi.org/10.1126/science.1197236.

Shi, Yunzhou, Delong Zhang, Terry B. Huff, Xiaofei Wang, Riyi Shi, Xiao-Ming Xu, and Ji-Xin Cheng. 2011. "Longitudinal in Vivo Coherent Anti-Stokes Raman Scattering Imaging of Demyelination and Remyelination in Injured Spinal Cord." *Journal of Biomedical Optics* 16 (10). https://doi.org/10.1117/1.3641988.

Tlili, M. M., M. Ben Amor, C. Gabrielli, S. Joiret, G. Maurin, and P. Rousseau. 2002. "Characterization of CaCO3 Hydrates by Micro-Raman Spectroscopy." *Journal of Raman Spectroscopy* 33 (1): 10–16. https://doi.org/10.1002/jrs.806.

Weiner, S., I. Sagi, and L. Addadi. 2005. "Choosing the Crystallization Path Less Traveled." *Science* 309 (5737): 1027–28. https://doi.org/10.1126/science.1114920.

Weiss, Ingrid Maria, Noreen Tuross, Lia Addadi, and Steve Weiner. 2002. "Mollusc Larval Shell Formation: Amorphous Calcium Carbonate Is a Precursor Phase for Aragonite." *Journal of Experimental Zoology* 293 (5): 478–91. https://doi.org/10.1002/jez.90004.

Yoreo, James J. De, Pupa U. P. A. Gilbert, Nico A. J. M. Sommerdijk, R. Lee Penn, Stephen Whitelam, Derk Joester, Hengzhong Zhang, et al. 2015. "Crystallization by Particle Attachment in Synthetic, Biogenic, and Geologic Environments." *Science* 349 (6247): aaa6760. https://doi.org/10.1126/science.aaa6760.

Zumbusch, Andreas, Gary R. Holtom, and X. Sunney Xie. 1999. "Three-Dimensional Vibrational Imaging by Coherent Anti-Stokes Raman Scattering." *Physical Review Letters* 82 (20): 4142–45. https://doi.org/10.1103/PhysRevLett.82.4142.

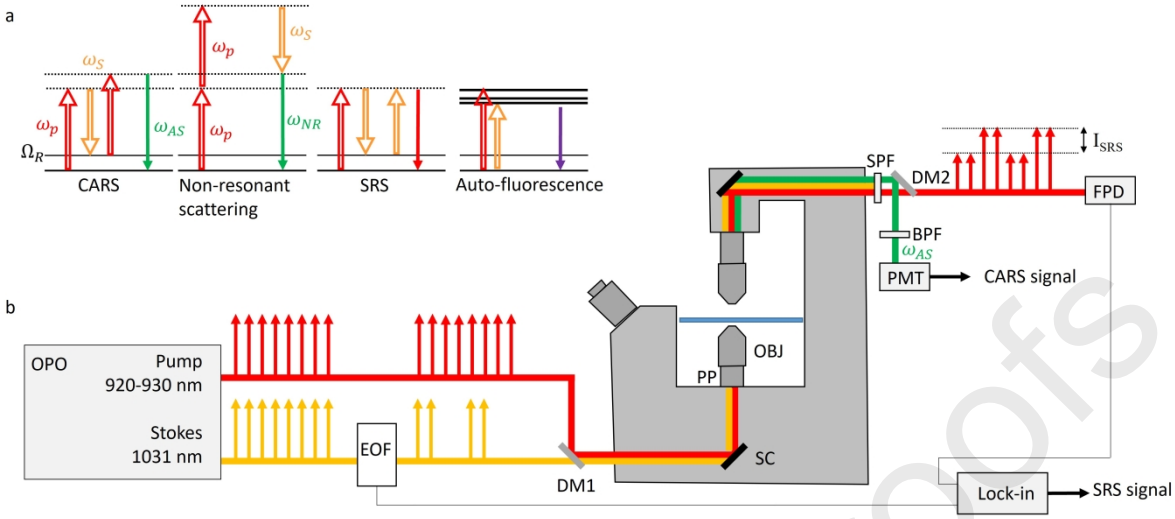

Figure 1: CARS/SRS setup a) Energetic diagram of the CARS, SRS, non-resonant scattering and auto-fluorescence processes. The empty arrows represent the photons coming from the lasers while the full arrows represent the photons emitted by the sample. The black lines and the dashed lines represent the vibrational levels and the virtual electronic levels, respectively. b) CARS/SRS experimental setup. OPO: optical parametric oscillators, EOF: Electro-Optical Frequency modulator (20MHz), DM1: Dichroic mirror to recombine pump and Stokes beams, SC: Scanning mirrors, PP: Piezo-positioner, OBJ: Objective (NA=0.75 ×20) mounted on a piezo. DM2: Dichroic mirror to separate the CARS photons from the lasers, BPF: Band pass filter to filter only the CARS photons, LPF Low pass filter to block the pump laser, PMT: Photo multiplier tube to count the CARS photons, FPD: Fast photo-diode to measure the laser intensity, Lock-in: Lock-in amplifier to recover the modulation due to the interaction with molecules of interest.

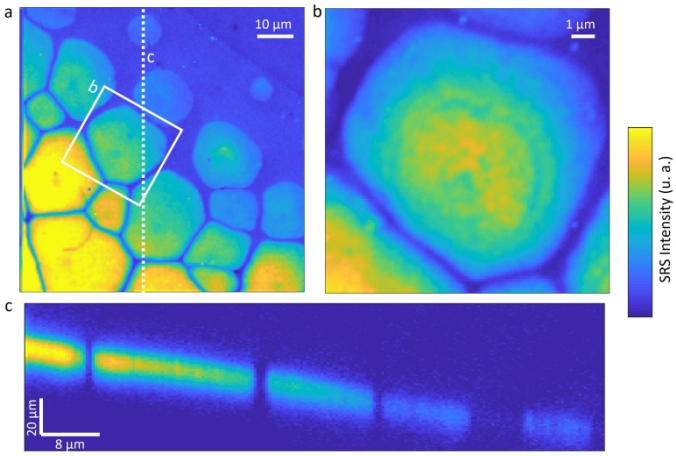

Figure 2: SRS images of a *Pinctada margaritifera* shell border obtained at 1086 cm^{-1}. a) Planar view, resulting from the integration of the 3D stack along the beam propagation direction. The dashed line corresponds to the perpendicular cut depicted in c. b) Zoom-in view of a young prism, depicted with a pixel size of 200 nm. Carbonate-poor ring structures are visible inside the prism, exhibiting a gap smaller than 1 µm. c) 2D cross section extracted from the 3D stack (highlighted by a white dashed line in a), evidencing the beam propagation direction, along the shell thickness. The axial resolution is lower than the lateral resolution with a typical value of a few µm.

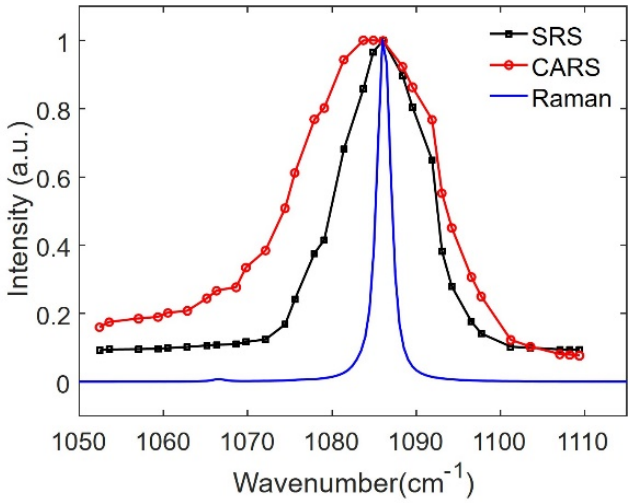

Figure 3: CARS/SRS/Raman spectra of a geological calcite crystal at ν_1. The ν_1 Raman spectrum presents a 2 cm^{-1} FWHM, directly related to the intrinsic dispersion of the chosen geological calcite. The natural FWHM of the SRS and CARS spectra are about 12 cm^{-1} and 18 cm^{-1}, respectively. The CARS and SRS spectra were acquired by changing the wavelength of the pump beam with steps of 0.2 nm

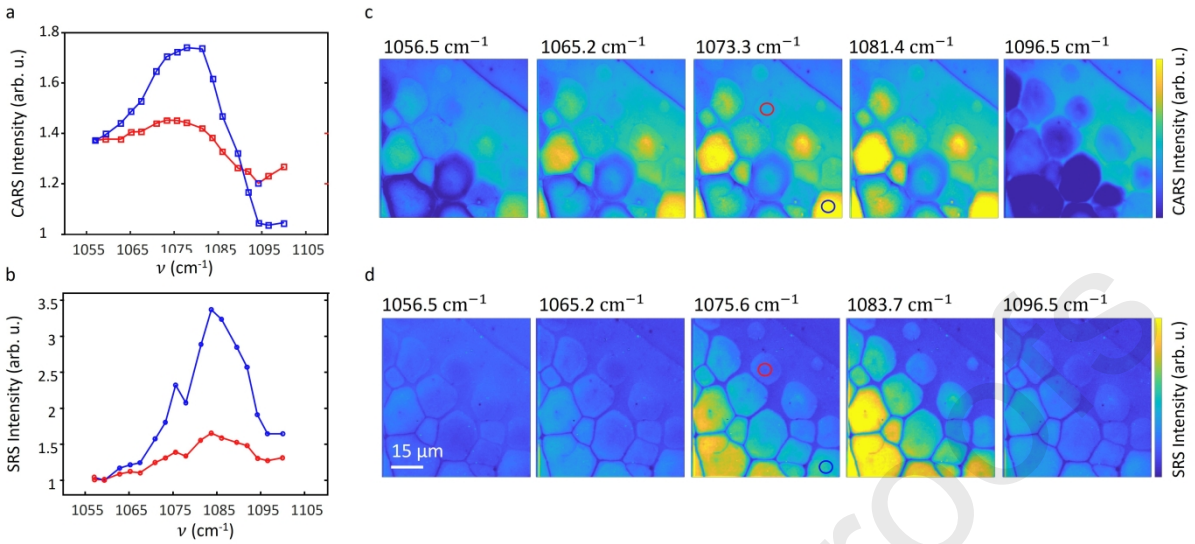

Figure 4: Hyperspectral images. a) CARS spectra extracted from two regions of interest, depicted in the CARS image obtained at 1073.3 cm^{-1}. The blue spectrum is recorded on a mature prism, while the red spectrum is recorded on a young disc. The CARS spectrum is strongly distorted due the interaction with the background. b) Same as a) for the SRS signal. The corresponding regions (*i.e.*, same disc and prism) are depicted on the SRS image obtained at 1075.6 cm^{-1}. On the lower wavenumber side, the spectra present a distortion with respect to the pure geological calcite (Fig 3). This asymmetric broadening denotes the presence of other carbonate polyamorphs. Both spectra are asymmetrically broadened, with however a more pronounced asymmetry for the disc spectra. c) Series of CARS images acquired for different wavenumbers values in the vicinity of υ_1. d) Same as c) for SRS imaging.

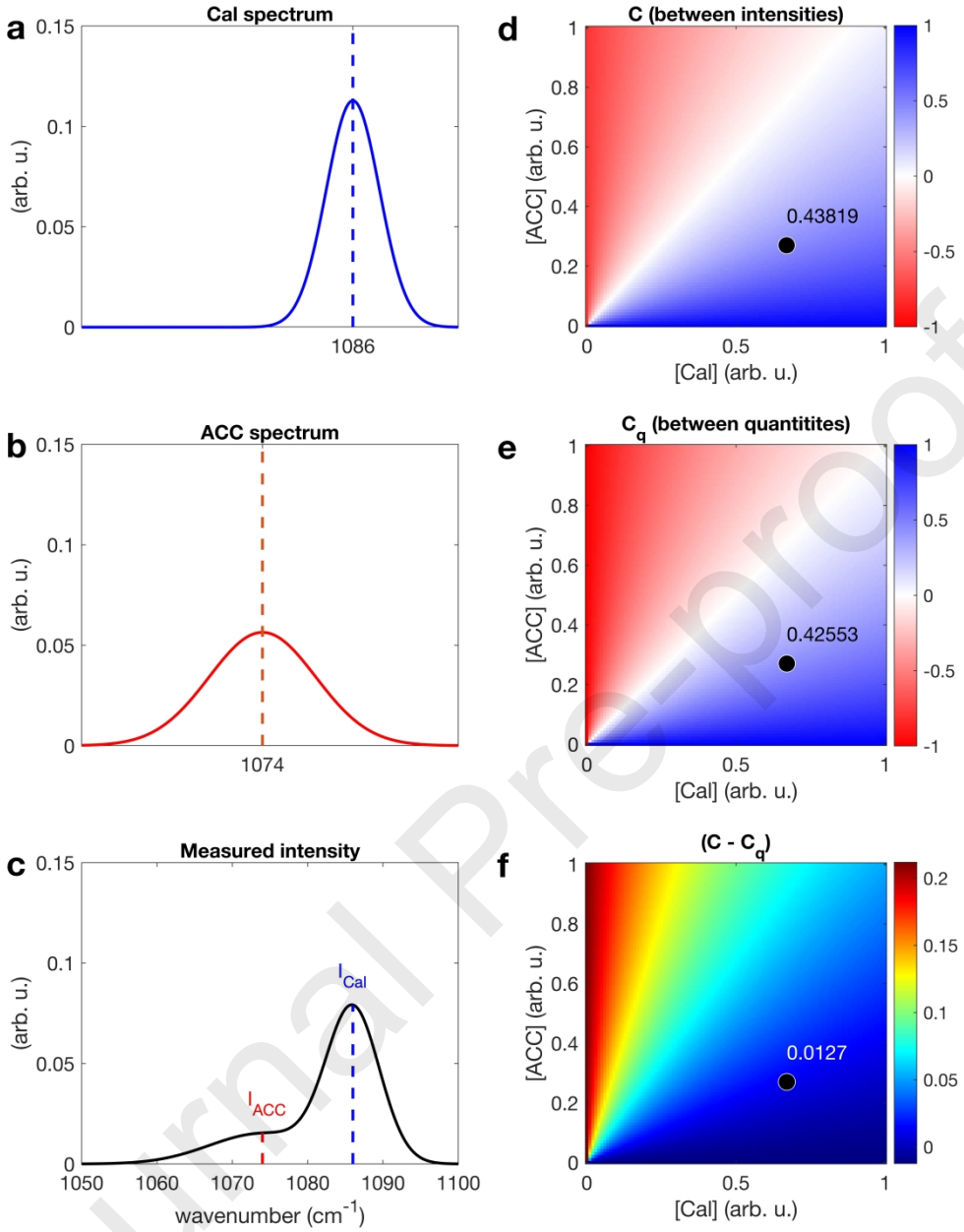

Figure 5. Numerical comparison of the C and C_q quantities. a) Simulated SRS spectrum of a pure calcite sample (Cal). b) Same as a) for a pure ACC sample. c) Theoretical spectrum of an arbitrary mixture of [Cal] and [ACC]. d) Colormap ratio C calculated from the SRS intensities taken at the Cal (1086 cm^{-1}) and ACC (1074 cm^{-1}) wavenumbers, plotted as a function of [Cal] and [ACC]. e) Same as d) for the C_q ratio, obtained from the true [Cal] and [ACC] concentrations. f) Colormap difference between the C and C_q maps. In d-f the black spot indicates the position corresponding to the spectra shown in a-c.

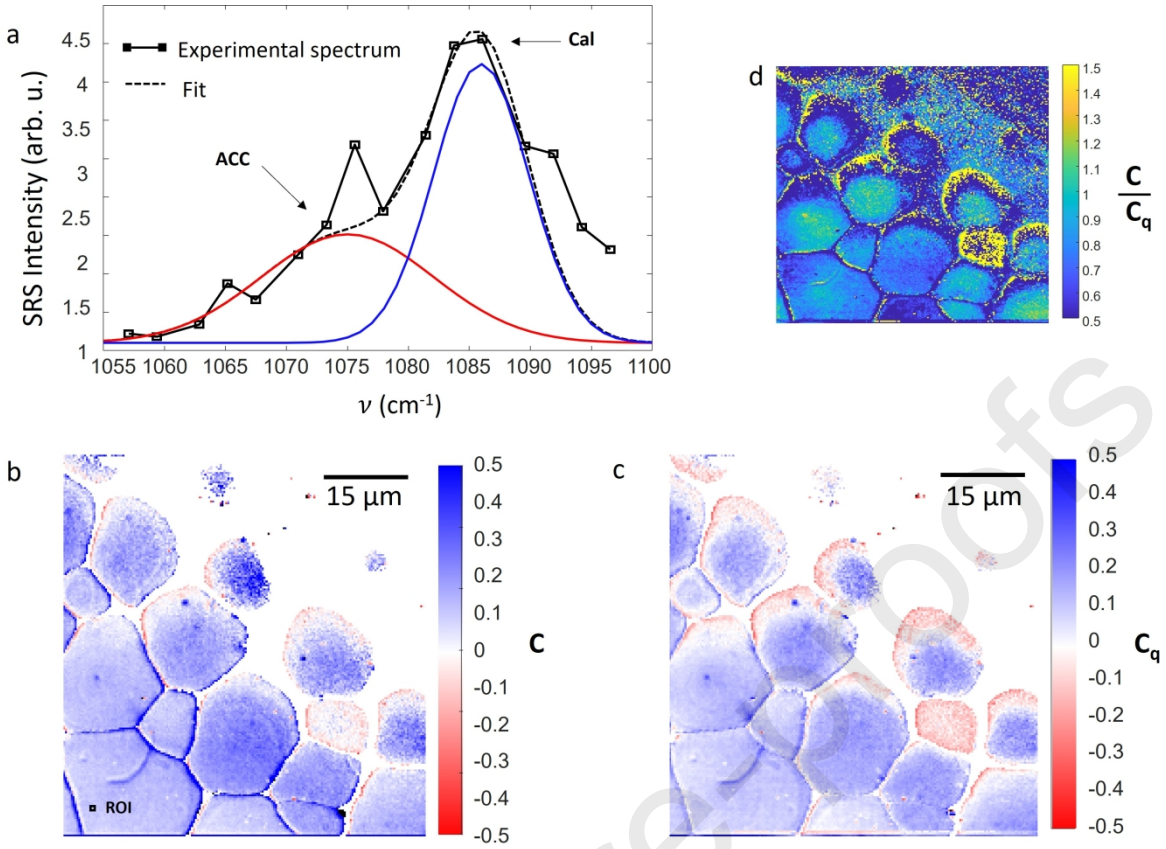

Figure 6: Experimental extractions of C_q. a) Experimental SRS spectrum from the region shown in b) (mature prism). The data has been fitted with a double-peak Gaussian profile (dashed line) corresponding to the Cal contribution (blue line) and the ACC contribution (red line) with standard deviations of 10 cm^{-1} and 20 cm^{-1} respectively. b) The C is calculated from the two image intensities taken at the Cal (1086 cm^{-1}) and ACC (1074 cm^{-1}) values depicted in a. c) The C_q is calculated using the amplitudes obtained for Cal and ACC from the fit procedure. d) Ratio between the two different contrast maps, showing less than 30% of variation.

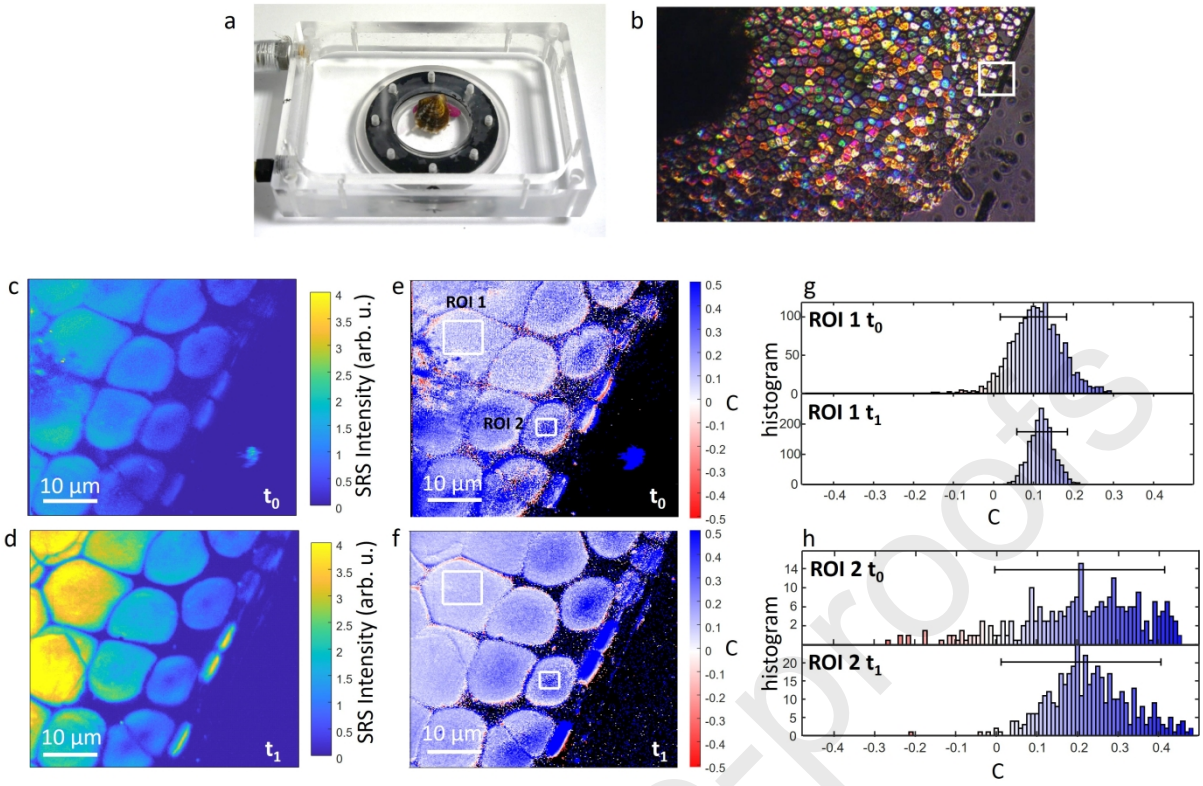

Figure 7: *in vivo* C ratio a) *In vivo* optically compatible cell containing the *Pm* oyster. The oyster is glued on a circular microscopic thin glass plate (150 µm thickness), fixed on the cell. The seawater is circulating into the cell thanks to two apertures, visible on the left side. b) White image of the border of the shell (between crossed polarizers). The absorbing part, on the left, corresponds to the animal, retracted into the shell. The white rectangle area (40 × 40 µm^2) corresponds to the region investigated with coherent Raman microscopy. c) SRS image at the Cal wavenumber, taken at t_0. d) Same as c, taken at $t_1 = t_0 + 3$days. Beside a global intensity increase, due to different incident laser powers, the difference between t_0 and t_1 seems marginal. e) C map, extracted for t_0. f) Same as e) for t_1. In c-f, the scale bar is indicated on the maps. g) Histograms of the C value from ROI 1 at t_0 and t_1. h) Same as g) from ROI2. In e) and g), the scale bars represent the C standard deviation calculated with eq. 6, from the statistics present in the Cal and ACC intensity images.

We certify that all authors have seen and approved the final version of the manuscript being submitted. They warrant that the article is the authors' original work, hasn't received prior publication and isn't under consideration for publication elsewhere.

Julien Duboisset (on behalf of the authors)

Declaration of interests

☒ The authors declare that they have no known competing financial interests or personal relationships that could have appeared to influence the work reported in this paper.

☐The authors declare the following financial interests/personal relationships which may be considered as potential competing interests: